OPTICS

Dual-function acoustic-to-optical transducers for underwater encrypted communication and subwavelength distance measurement

Xiao Yu[1]†, Jiaxuan Zhou[1]†, Zhiyao Zhang[1], Liangliang Lu[1,2]*, Xingsheng Luan[3], Chong Sheng[1,4]*, Shining Zhu[1], Hui Liu[1]*

The development of next-generation communication networks with integrated multifunctional capabilities across diverse environments—spanning space, air, land, and sea—requires efficient transduction between disparate information carriers. While substantial progress has been made in transducers for terrestrial applications, devices that unify sensing and communication in underwater environments remain in their infancy. We present an experimental demonstration of a dual-function acoustic-to-optical transducer, enabling simultaneous underwater encrypted communication and distance measurement. Specifically, the transducer efficiently converts underwater acoustic signals into single photons for transmission through optical fibers over distances of up to 50 kilometers. Concurrently, we achieve deep subwavelength precision in distance measurement, reaching an accuracy of 1/250 of the acoustic wavelength, while maintaining robust communication performance. Furthermore, we implement coincidence counting–based encryption to embed acoustic information within noisy optical fiber networks. This work represents a notable step toward next-generation network architectures that seamlessly integrate sensing and communication across heterogeneous media.

INTRODUCTION

With the advancement of modern communication networks, the development of an integrated communication system encompassing space, air, land, and sea has become imperative. Hybrid communication networks (*1*), capable of managing and transforming vast datasets, have played a pivotal role in this context. Among these, transducers (*2*–*7*) that enable the conversion of information between various carriers are critical components within hybrid communication networks. A notable example is quantum communication networks (*8*–*10*), which may manipulate information at frequencies up to several gigahertz and distribute it via optical fibers at frequencies up to hundreds of terahertz. Notably, all the aforementioned information carriers operate within the electromagnetic spectrum. However, electromagnetic waves are not universally suitable for information transmission in all environments. For instance, in underwater communication networks (*11*), the strong absorption of electromagnetic waves in water makes acoustic waves the primary carriers. Existing optical fiber communication networks are indispensable tools for information transmission in modern communication systems. Consequently, transducers (*12*) capable of converting underwater acoustic information into optical fiber are crucial components in the development of integrated space-air-ground-sea communication networks.

In addition to communication, sensing constitutes another fundamental functionality within the next-generation communication networks (*13*). Among the physical quantities perceived, distance sensing has garnered considerable attention due to its high demand for accurately positioning information sources. In addition, great advances have been made into distance sensing using optical and acoustic methods (*14*–*16*). Moreover, one can leverage nonclassical attributes of light (*17*–*21*) to extend the sensitivity of distance measurement. Notably, there has been growing interest in integrating distance sensing and communication functionalities into a unified platform (*22*), indicating that a transducer can concurrently convey information and determine the location of the information source. However, the dual-function transducer, which combines sensing and communication capabilities, remains in its infancy within the underwater environment.

At the same time, fiber optical microcavities (*23*), including Fabry-Pérot cavities, phase-shifted Bragg gratings, and whispering gallery mode microcavities, have garnered widespread attention for their application in sound sensing and detection (*24*–*27*). Examples include hydrophones (*28*–*30*), ultrasonic imaging (*31*–*33*), photoacoustic spectroscopy (*34*), seismic detection (*35*, *36*), as well as acoustic source localization (*37*–*39*). Beyond acoustic sensing, these microcavities can also serve as transducers for voice signal sensing (*40*), effectively converting acoustic information into optical signals. However, with the rise of quantum networking, there is growing interest in quantum-level information conversion between distinct carriers using transducers (*2*, *5*, *6*). To date, few studies have focused on acoustic-to-optical transducers that convert classical acoustic information into optical signals at the single-photon level.

In this work, we demonstrate the experimental realization of a dual-function acoustic-to-optical transducer capable of simultaneous distance sensing and communication in underwater environments. The transducer is constructed through the integration of an optomechanical Fabry-Pérot cavity at the end of an optical fiber. Our experimental results indicate that this transducer exhibits high efficiency in sonic sensitivity, facilitating the effective conversion of underwater acoustic signals into single photons within the optical

[1]National Laboratory of Solid State Microstructures and School of Physics, Collaborative Innovation Center of Advanced Microstructures, Nanjing University, Nanjing, Jiangsu 210093, China. [2]Key Laboratory of Optoelectronic Technology of Jiangsu Province, School of Physical Science and Technology, Nanjing Normal University, Nanjing, Jiangsu 210023, China. [3]State Key Laboratory of Quantum Optics Technologies and Devices, and Institute of Opto-Electronics, Shanxi University, Taiyuan, 030006, Shanxi Province, China. [4]Jiangsu Key Laboratory of Quantum Information Science and Technology, Nanjing University, Suzhou, Jiangsu 215163, China.
*Corresponding author. Email: liangliangl u@nju.edu.cn (L.L.); csheng@nju.edu.cn (C.S.); liuhui@nju.edu.cn (H.L.)
†These authors contributed equally to this work.

fiber. We thereby demonstrate the capability to transmit this acoustic information over distances up to 50 km using single photons. Besides transmitting and distributing acoustic information, we also use the time-correlated single-photon counting (TCSPC) technique for the precise localization of acoustic sources, achieving accuracy to within 1/250 of the acoustic wavelength. Furthermore, we use coincidence-counting techniques for correlated photon pairs to retrieve acoustic-modulated single photons information within noisy optical fiber networks. These findings offer a promising approach to interlinking and interpreting information across diverse media, contributing substantially to the integrated sensing and communication networks.

RESULTS

Acoustic sensors by an optomechanical fiber Fabry-Pérot cavity

To achieve the conversion of acoustic signals into optical waves, we use an optomechanical fiber Fabry-Pérot cavity (OMFPC) as a transducer. As illustrated in Fig. 1B, the transducer is composed of the end face of an optical fiber and a reflective polyethylene terephthalate (PET) membrane coated with silver, forming a Fabry-Pérot cavity. The cavity is mechanically reinforced by a ceramic ferrule and an aluminum sleeve, while a quarter-pitch graded-index multimode fiber is integrated to collimate the optical beam, thereby minimizing divergence losses within the cavity (note S4). The interference spectrum of the OMFPC, shown in Fig. 1C, exhibits a free spectral range (FSR) of 5.8 nm and a maximum extinction ratio of 19.3 dB. When an acoustic wave impinges on the PET diaphragm, it induces mechanical vibrations that alter the cavity length. This change in cavity length results in a phase shift, which, in turn, causes a corresponding shift in the interference pattern (note S1). To optimize the acoustic response, the operating optical wavelength is tuned to the quadrature point on one linear region of the interference spectrum, as depicted in Fig. 1D. Figure 2 presents the acoustic response characteristics of this OMFPC. In experiments, a piezoelectric transducer (PZT) is used to generate an acoustic signal underwater, and the output pressure is calibrated with a standard hydrophone to ensure precise and repeatable control of the sound amplitude. The OMFPC was then immersed in a water tank under controlled laboratory conditions to receive the transmitted acoustic signal. The sensor output demonstrates high linearity with respect to varying sound pressure levels, as shown in Fig. 2A. In the present study, acoustic sensitivity is defined as the ratio of the phase shift $\Delta\phi$ (in radians) of the interference fringes in the reflection spectrum to the corresponding applied pressure ΔP (in pascals), expressed as $S = \Delta\phi/\Delta P$. Also, $\Delta\phi$ is calculated as $\Delta\phi = 2\pi\frac{\Delta\lambda}{\mathrm{FSR}}$, which is the ratio between the measured wavelength shift $\Delta\lambda$ and the FSR of the cavity. The frequency response, as

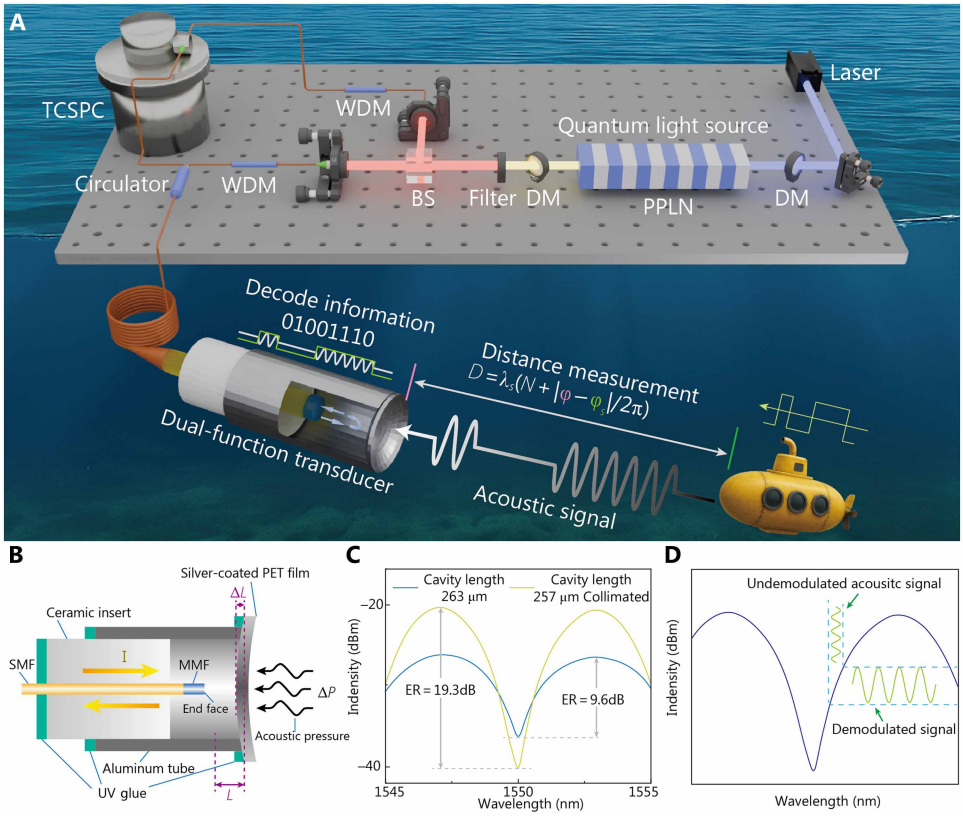

Fig. 1. Schematic of a dual-function acoustic-to-optical transducer at the single photon level. (**A**) Diagram of the single-photon acoustic signal conversion and the distance measurement. (**B**) Schematic diagram of the internal structure of this OMFPC. (**C**) Comparison of the reflection spectra of this cavity before and after incorporating the collimation structure. (**D**) Diagram illustrating the principle of signal transmission with the working wavelength tuned to the quadrature point of the linear region of the interference spectrum. PPLN, periodically poled lithium niobate; UV, ultraviolet; BS, beam splitter; DM, dichroic mirror; WDM, wavelength division multiplexing; SMF, single-mode fiber; MMF, multimode Fiber; ER, extinction ratio.

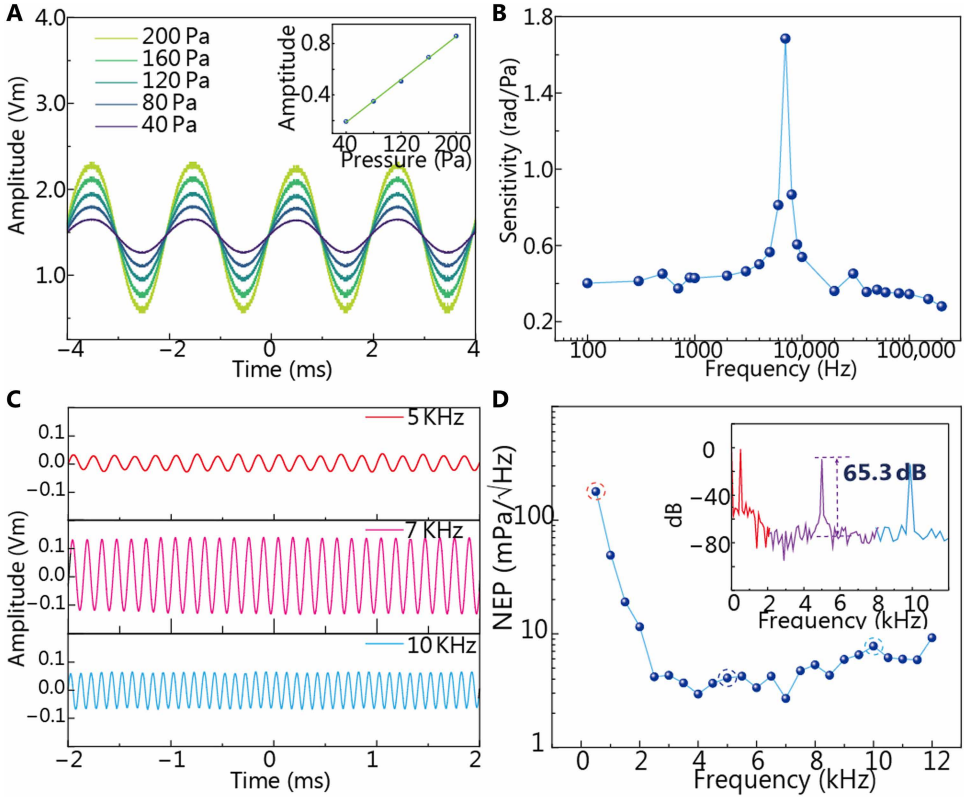

Fig. 2. Acoustic response characteristics of the OMFPC. (**A**) Linear response of this cavity to varying sound pressure levels. (**B**) Frequency response showing a resonance peak at ~7 kHz with a sensitivity of 1.7 rad/Pa. (**C**) Time-domain response of a sinusoidal signal at different frequencies. (**D**) Noise equivalent pressure spectrum with a minimum value of 1.713 mPa/$\sqrt{\text{Hz}}$ at the resonant frequency and a signal-to-noise ratio exceeding 60 dB exhibited in the inset.

shown in Fig. 2B, exhibits a distinct resonance peak at around 7 kHz and a corresponding sensitivity of about 1.7 rad/Pa. This resonant behavior is further confirmed by the time-domain response of a sinusoidal signal at different frequencies in Fig. 2C, which shows the maximum signal amplitude for the resonant frequency. The noise equivalent pressure (NEP) spectrum of the system is presented in Fig. 2D. At the resonant frequency, the NEP achieves a minimum value of ~1.713 mPa/$\sqrt{\text{Hz}}$, with a measured signal-to-noise ratio exceeding 60 dB, demonstrating the system's low-noise and high-resolution acoustic sensing capabilities. Notably, while the present acoustic sensor demonstrates high sensitivity, its bandwidth is constrained to only 100 kHz. Nevertheless, substantial bandwidth enhancement can be achieved by optimizing the optical Fabry-Pérot cavity (*41*) or by adopting alternative optical cavity configurations (*42*).

Acoustic information conversion using quantum nonlocal effects

After transducing acoustic signals to optical signals via the OMFPC, we harness quantum nonlocal effects of entangled photons to manipulate acoustically modulated single photons. Photon pairs are generated by type 0 parametric downconversion in a periodically poled lithium niobate crystal (note S2D). The output state can be expressed as $\int d\omega_s d\omega_i\, C(\omega_s, \omega_i)\,|\omega_s, \omega_i\rangle$, where $C(\omega_s, \omega_i)$ denotes the joint spectral amplitude, exhibiting strong frequency anticorrelation between the signal (ω_s) and idler (ω_i) photons such that $\omega_s + \omega_i = \omega_p$. A coarse wavelength division multiplexer (CWDM) separates the signal and idler photons into two paths: Idler photons are directed to a reference path, while signal photons are routed to a probe path for acoustic modulation (Fig. 3A). Conventional acoustic sensing typically requires probe photons to operate within the linear region of the Fabry-Pérot cavity's interference spectrum. Contrary to classical approaches, we place the optical band-pass filter not in the signal path but counterintuitively in the idler path. This approach is akin to quantum ghost imaging, which exploits correlations between two spatially separated light fields to reconstruct an image using photons that never interact with the object.

To experimentally demonstrate the conversion of underwater acoustic signals into single photons with quantum nonlocal effects, we encode an "NJU" signal sequence using amplitude-shift keying (ASK) at an acoustic carrier frequency of 12 kHz (see note S5 for acoustic modulation details). Reconstruction of the acoustic information via nonlocal optical filtering in the idler path is shown in Fig. 3B. A demultiplexer (DEMUX) divides the available single-photon spectrum into up to four spectral channels within the telecommunication band, each with a full width at half maximum bandwidth of 0.4 nm and a channel spacing of 0.8 nm. Through optical routing, idler photons from different wavelength channels and the acoustically modulated signal photons are separately detected by commercially available superconducting nanowire single-photon detectors (SNSPDs) for coincidence counting. Figure 3C presents experimental results on extracting acoustic information by varying the central wavelength of band-pass filters placed in the path of the idler photons, which do not interact with the acoustic wave. For example, when the band-pass filter for the idler photons is set to C34—a wavelength

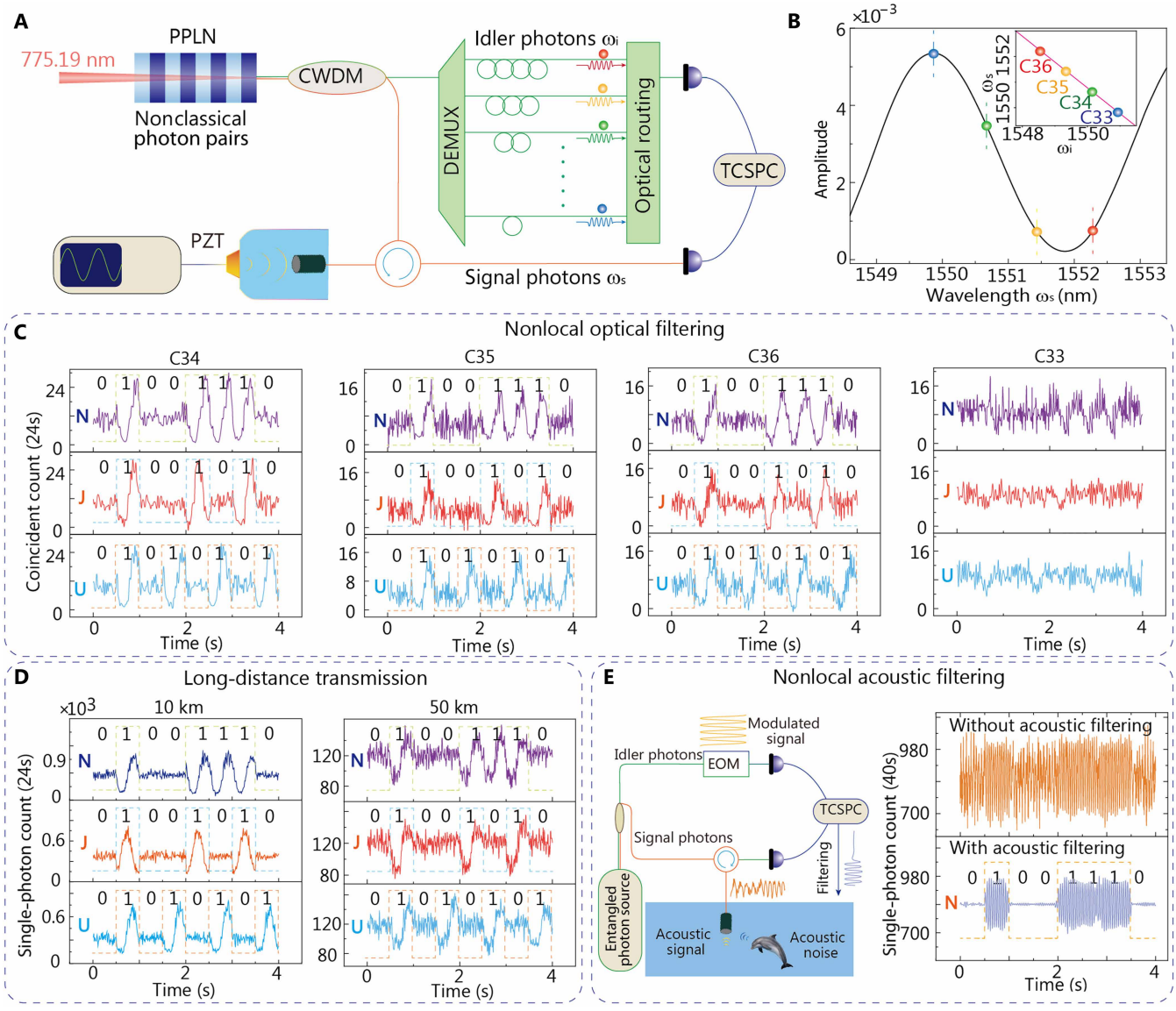

Fig. 3. Signal reconstruction and distribution of acoustic information using quantum nonlocal effects. (**A**) The schematic of quantum nonlocal effects to extract acoustic information from the non-interaction single idler photons using wavelength division multiplexing. (**B**) The spectrum of the FP cavity in the signal-photon path. The inset illustrates frequency anticorrelation between the signal and idler photons. (**C**) ASK-coded signals are reconstructed in multichannels via quantum nonlocal effect and wavelength division multiplexing. (**D**) The NJU signals after transmission through 10- and 50-km fiber spools in the controlled experiment. (**E**) Quantum nonlocal effects to realize acoustic filtering. AWG, arbitrary waveform generator. C33 to C36 are wavelength channels designated by the International Telecommunication Union.

channel designated by the International Telecommunication Union—its central wavelength is 1550.116 nm. Given the frequency anticorrelation relation ($\omega_s + \omega_i = \omega_p$), this configuration is equivalent to placing a band-pass filter with a central wavelength of 1550.63 nm in the signal-photon path. This equivalent wavelength lies within the linear region of this Fabry-Pérot cavity (Fig. 3B), enabling the extraction of acoustic information. In contrast, when band-pass filters C35 or C36 are used for the idler photons, the acoustic information becomes degraded because the corresponding equivalent wavelengths deviate from the linear operating region. Notably, when filter C33 is used, the equivalent wavelength falls completely outside the linear region, making it impossible to extract any acoustic information.

In addition to nonlocal optical filtering, we also implement nonlocal acoustic filtering by manipulating single photons in the reference path. In this experiment, the target acoustic carrier remains at 12 kHz, while an additional 8-kHz tone is intentionally introduced as environmental noise. Consequently, the demodulated acoustic signal becomes corrupted (Fig. 3E). By modulating the idler photons with an electro-optic modulator (EOM) driven at the same frequency as the acoustic carrier, we successfully retrieve the original acoustic information after data processing.

Furthermore, we demonstrate long-distance distribution of acoustic information at the single-photon level over optical fiber. All experiments were conducted in a stable laboratory environment using spools of 10-km and 50-km single-mode optical fiber. Despite propagation

losses, the modulated signal remains clearly distinguishable from noise after 10- and 50-km transmission, as shown in Fig. 3D.

Distance measurement with the precision of subacoustic wavelength

Beyond acoustic communication, we harness TCSPC technology to endow the transducer with subwavelength ranging capability toward an acoustic source. Because the PZT emits a single-frequency sinusoidal acoustic wave, we adopt a phase-based ranging method to determine the distance between the source and the sensor

$$D = \lambda_s\left(N + \frac{\Delta\varphi}{2\pi}\right) \quad (1)$$

where λ_s is the acoustic wavelength, $\Delta\varphi$ denotes the phase difference, and N represents the integer number of full periods. To resolve the ambiguity in determining N, we synchronize the PZT with the EOM in the idler-photons path (Fig. 4A). Moreover, the TCSPC time-tagging capability, combined with the sinusoidal modulation profile, then allows precise extraction of $\Delta\varphi$. Since each acoustic signal encodes a unique initial phase, phase variations ($\Delta\varphi = \varphi - \varphi_s$) translate directly into relative displacement ΔD through $\Delta D = \lambda_s\Delta\varphi/2\pi$. This strategy integrates TCSPC's fine timing resolution with quantum-assisted signal reconstruction algorithms to recover the sinusoidal waveform and track its phase evolution with high fidelity (Methods and note S2).

In experiments, the information generated by the acoustic source is modulated via sinusoidal wave trains, which are recorded at various spatial positions. As illustrated in Fig. 4B, the sinusoids reconstructed via the quantum algorithm faithfully decode the phase-delay information. The displacements between the OMFPC and the acoustic source, computed from the phase shifts of the reconstructed acoustic signals, agree closely with the actual physical displacements (Fig. 4C). To quantify the ranging resolution of our approach, we performed systematic measurements under well-controlled conditions. The statistical distribution of the data (Fig. 4D) reveals a resolution of about 0.5 mm. Notably, this subwavelength precision at an operating acoustic wavelength of $\lambda_s \approx 125$ mm enables the localization of the acoustic source with an accuracy of $\lambda_s/250$.

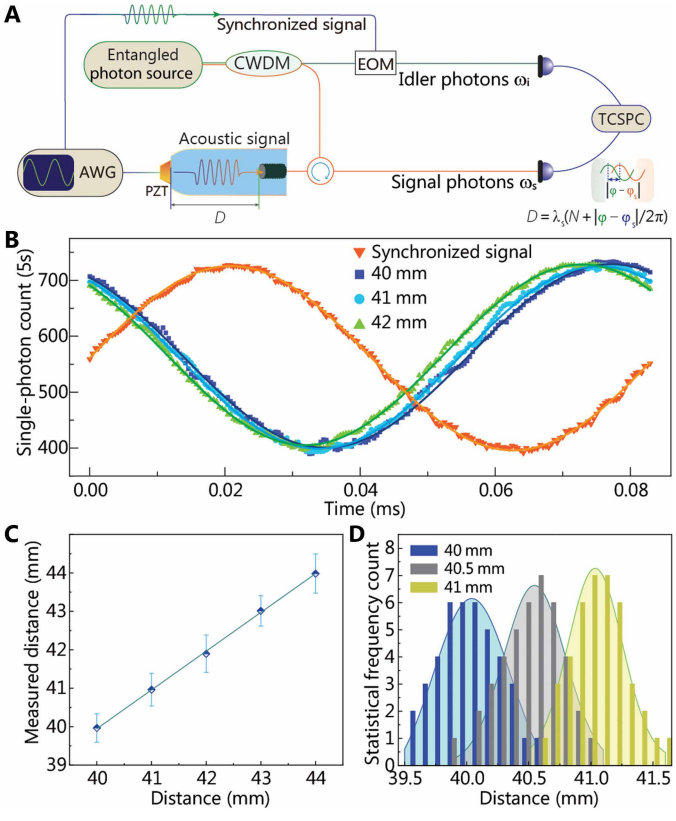

Fig. 4. Subwavelength distance measurement. (**A**) The schematic of distance measurement. Synchronization is established through a common AWG. The AWG output is divided into two channels: The first channel gates an EOM to impress timing markers on idler photons, yielding a reference signal; the second channel excites a PZT to emit the acoustic signal for underwater ranging. (**B**) Phase shift of sinusoidal signals at different positions. (**C**) The comparison between experimentally measured distances and actual values. (**D**) Statistical distribution of measured distances, indicating a resolution of ~0.5 mm.

The encryption for acoustic information within optical fiber networks

In communication networks, information encryption serves as a critical tool to ensure information security. To protect the transmission of acoustic information against unauthorized eavesdropping, we introduce a classical light source as white noise within fiber optic networks, as illustrated in Fig. 5A. If the eavesdropper only detects acoustic-modulated single photons without reference single photons, the decoded acoustic information is submerged in a noisy background, just as shown in Fig. 5C. In contrast, we can decrypt this acoustic information from environmental noise by coincidence detection between acoustic-modulated and reference single photons. Specifically, a coincidence detection event is defined as a detection event on the reference detector at time t_r being followed by another detection event on the probe detector at time t_p after routing through the OMFPC, such that $t_p - t_r$ lies within a small coincidence window as follows

$$t_p - t_r \in \left[(l_p - l_r)/c - \Delta T_c/2, (l_p - l_r)/c + \Delta T_c/2\right] \quad (2)$$

where ΔT_c is the temporal width of the coincidence window and l_p (l_r) is the optical path length of the probe (reference) photons, c is the speed of light. We further quantify the measurement precision of acoustic-modulated probe single photons using the Fisher information (*17*–*19*), which characterizes the amount of information about the true signal embedded in the observed data. The Fisher information I is expressed as (see note S3 for details)

$$I = \left(\frac{\eta_r^2 f^2}{P_c} + \frac{(1-\eta_r^2)f^2}{f_b + \eta_p f - P_c} + \frac{\eta_r^2 f^2}{\eta_r f - P_c}\right)\tau \quad (3)$$

where f (f_b) is the output flux of probe (noise) photons, η_r (η_p) is the transmission efficiency of the reference (probe) photons, τ is the measurement time, $P_c = \eta_r\eta_p f + \eta_r f_b f\,\Delta T_c$ is the coincidence detection rate. The first term in the expression represents the contribution of coincidence detection P_c to the Fisher information, and the last two terms represent the contribution of noncoincident detection rate. In the presence of strong background noise, the contribution from coincidence detection dominates the total Fisher information. This arises because noise photons predominantly enhance noncoincident probe detection rate, while their impact on the coincidence detection rate

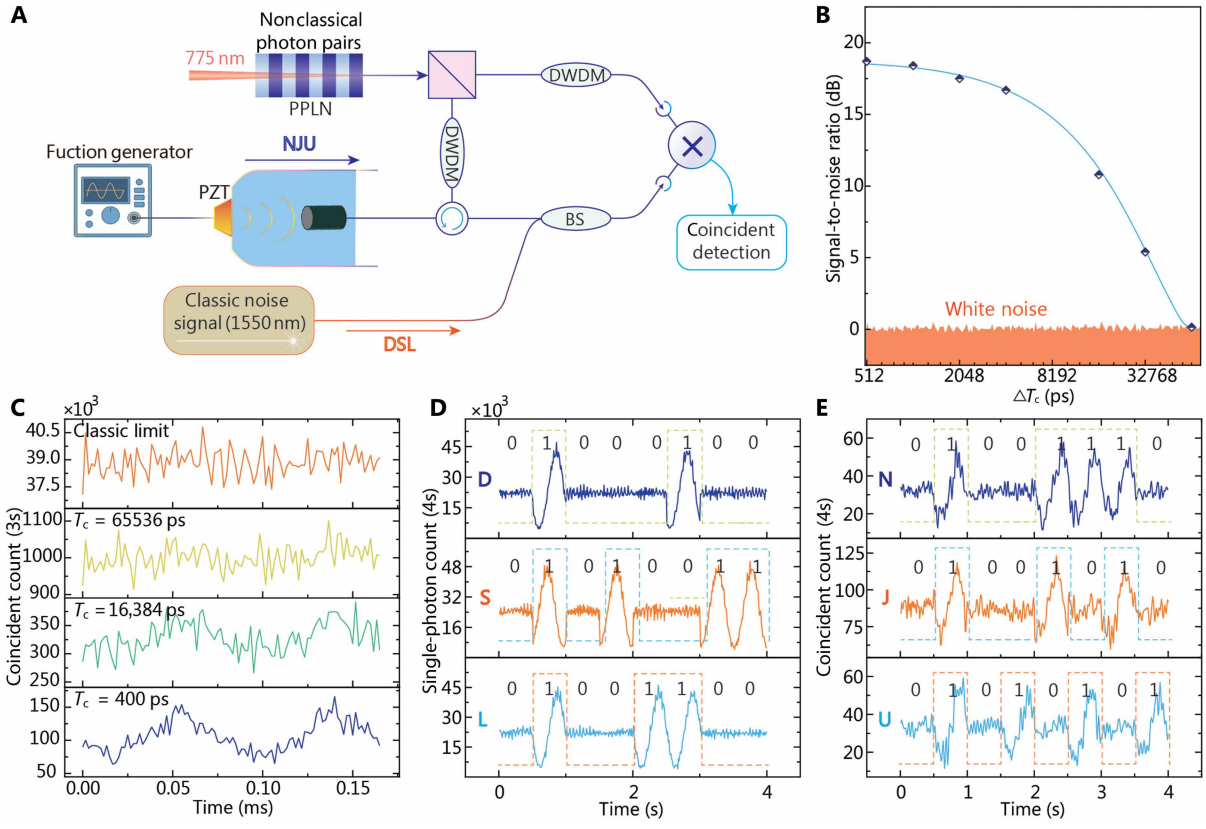

Fig. 5. The encrypted information within noisy optical fiber networks. (**A**) Schematic of introducing a classical light source as noise within fiber optic networks. (**B**) Signal-to-noise ratio as the temporal width of the coincidence window. (**C**) The suppression of noise using coincident detection by reducing coincidence window width. (**D**) The detection of false information DSL using single probe photons counts. (**E**) The decrypted information NJU by coincidence detection of the probe photons and reference photons.

P_c is constrained by the narrow coincidence window ΔT_c. Therefore, the amount of information about the true signal increases as the coincidence window narrows.

In experiments, by reducing the temporal width ΔT_c, we can progressively suppress noise contamination and gradually obtaining real acoustic-modulated single photon signals, as demonstrated in Fig. 5C. In our current experimental setup, the coincidence window is limited by the detector's temporal resolution, yielding a maximum signal-to-noise ratio of ~17.5 dB at $\Delta T_c = 400$ ps (see Fig. 5B). Improving the detector's temporal resolution could further enable high-precision decryption of acoustic-modulated single photon signals. Beyond hiding information in noise, we can modulate classical light sources to transmit false information (see Fig. 5A), thereby deceiving potential eavesdroppers. If the eavesdropper only measures the probe single photons, they obtain the information "DSL," as illustrated in Fig. 5D. In contrast, the authentic acoustic-modulated information NJU can only be revealed through coincidence detection of the probe photons and reference photons. Notably, the successful extraction of acoustic-modulated information from noisy backgrounds critically depends on a noise-free reference path. Unlike signal photons, which experience extended fiber propagation and acoustic modulation, reference photons are stored locally, avoiding the additional noise introduced by long-distance transmission and external modulation. This local storage ensures a comparatively clean noise environment.

DISCUSSION

In this study, we present a fiber-based Fabry-Pérot transducer that enables the transfer of encoded information from an acoustic carrier to an electromagnetic carrier. Moreover, we extend the concept to facilitate information carrier conversion from classical acoustic signals to encrypted single-photon states. This breakthrough offers a pathway for integrating classical underwater communication networks with quantum communication systems, thereby opening new frontiers in advanced communication technologies. Beyond its communication applications, the same optical fiber Fabry-Pérot cavity is used for achieving subacoustic-wavelength distance measurements, attaining a precision of 1/250 of the sound wavelength while simultaneously maintaining communication functionality. This dual-purpose capability provides a foundation for integrated sensing communication systems, with potential applications across space, aerial, terrestrial, and underwater environments. The current implementation uses three wavelength channels of an optical-fiber Fabry-Pérot cavity to distribute acoustic information and locate the acoustic source. Future directions include the integration of more Fabry-Pérot cavities, the multiplexing of more photonic degrees of freedom (e.g., time, polarization, and path), and the utilization of low-noise quantum light sources (e.g., squeezed vacuum states) to increase the number of information distribution channels and improve the precision of acoustic source localization.

Currently, coincidence counting based on single photons is hindered by the limited brightness of quantum light sources, resulting

in long averaging times and low quantum transmission rates (~60 bps) relative to classical light. Nevertheless, enhancing the generation rate of photon pairs and reducing scattering loss in optical fiber Fabry-Pérot cavities are promising approaches to substantially reduce these averaging times. Specifically, the current generation rate of photon pairs is ~100 kHz, whereas state-of-the-art quantum light sources have achieved rates of about 1 MHz, which could substantially decrease the averaging time. In addition, light propagating through an optical fiber Fabry-Pérot cavity typically experiences a loss of ~13 dB, primarily caused by scattering from the uneven fiber end face and reflective coatings. Reducing this scattering loss would also contribute to shortening the averaging time.

In general, acoustic sensing now relies on two principal technologies: conventional PZTs and optical acoustic sensors. While PZTs convert sound signals into electrical outputs, their operation is inherently incompatible with all-optical fiber networks. Alternative optical approaches, such as π-phase–shifted Bragg gratings and whispering-gallery-mode (WGM) microcavities, can transduce acoustic signals into optical domains for optical communications; however, they face substantial practical constraints. Specifically, π-phase–shifted Bragg gratings require femtosecond laser direct writing techniques, and WGM microcavities depend on high-precision nanofabrication methods including electron beam lithography or deep-ultraviolet photolithography. These intricate nanofabrication processes inevitably escalate device cost and complexity. Moreover, WGM structures—such as microspheres and microdisks—are challenging to integrate seamlessly with standard optical fiber infrastructure. In contrast, fiber-based Fabry-Pérot cavities, fabricated directly on the fiber tip, combine low-cost fabrication with straightforward integration into existing optical fiber networks, offering a compelling alternative for practical acoustic-to-optical transducers in encrypted communication. Despite the ease of fabrication of fiber-based Fabry-Pérot cavities, acoustic sensors based on such cavities face challenges in further miniaturization and large-scale deployment. Fortunately, a sensitive, compact, broadband, and scalable acoustic sensor (*43*) based on silicon photonics—fabricated through complementary metal-oxide semiconductor–compatible processing—offers a solution to this challenge.

METHODS

Single-photon acoustic signal reconstruction algorithm

In the present work, we use a quantum light source to replace the classical light source for the reconstruction of acoustic signals. In experiments, we use a superconducting nanowire SNSPD to receive single-photon signals. The SNSPD converts each detected single-photon signal into an electrical pulse, which is then recorded by a TCSPC module. This module records each photon event, including the photon arrival time and channel information. The model of the TCSPC module we use is the PicoHarp300, which has a minimum time channel width of 4 ps.

To retrieve the acoustic wave period for a given frequency of the acoustic wave, we divide the acoustic wave period into a series of small sampling cycles at equal intervals. The TCSPC module records the photon arrival times and their corresponding channel information within these sampling cycles. We perform coincidence counting on the photon events within each sampling cycle and record the coincidence counts. For an acoustic wave period comprising a series of sampling cycles, we obtain a series of coincidence counts. Since our ASK signal contains binary "0" and "1" information, each binary 1 signal consists of multiple identical acoustic wave periods. Therefore, we can sum the coincidence counts of corresponding sampling cycles across different acoustic wave periods to reconstruct the sinusoidal waveform representing the 1 signal. Ultimately, the waveform of the binary 1 signal can be equivalently represented by the waveform of a single acoustic wave period. In addition, we take a 10-kHz acoustic wave as an example, if a binary 1 signal pulse lasts 1 s, the signal will contain 10,000 acoustic wave periods, each with a duration of 0.1 ms. We divide each acoustic wave period into 200 sampling cycles at equal intervals, resulting in each sampling cycle having a duration of 0.5 μs. We denote the coincidence count recorded by the TCSPC in the ith sampling cycle of the jth acoustic wave period as n_{ij}. Then, for all 10,000 acoustic wave periods, the coincidence counts of the 10,000 sampling cycles at the same sampling position can be accumulated as $N_i = \sum_j n_{ij}$. Last, we reconstruct a sinusoidal waveform with 200 sampling points, which represents the binary 1.

Supplementary Materials

This PDF file includes:

Supplementary Text
Figs. S1 to S13
Table S1
References

REFERENCES

1. X. You, C.-X. Wang, J. Huang, X. Gao, Z. Zhang, M. Wang, Y. Huang, C. Zhang, Y. Jiang, J. Wang, M. Zhu, B. Sheng, D. Wang, Z. Pan, P. Zhu, Y. Yang, Z. Liu, P. Zhang, X. Tao, S. Li, Z. Chen, X. Ma, C.-L. I, S. Han, K. Li, C. Pan, Z. Zheng, L. Hanzo, X. Shen, Y. J. Guo, Z. Ding, H. Haas, W. Tong, P. Zhu, G. Yang, J. Wang, E. G. Larsson, N. H. Quoc, W. Hong, H. Wang, D. Hou, J. Chen, Z. Chen, Z. Hao, G. Y. Li, R. Tafazolli, Y. Gao, H. V. Poor, G. P. Fettweis, Y.-C. Liang, Towards 6G wireless communication networks: Vision, enabling technologies, and new paradigm shifts. *Sci. China Inf. Sci.* **64**, 110301 (2021).
2. R. W. Andrews, R. W. Peterson, T. P. Purdy, K. Cicak, R. W. Simmonds, C. A. Regal, K. W. Lehnert, Bidirectional and efficient conversion between microwave and optical light. *Nat.Phys.* **10**, 321–326 (2014).
3. K. Fang, M. H. Matheny, X. Luan, O. Painter, Optical transduction and routing of microwave phonons in cavity-optomechanical circuits. *Nat. Photonics* **10**, 489–496 (2016).
4. W. Jiang, C. J. Sarabalis, Y. D. Dahmani, R. N. Patel, F. M. Mayor, T. P. McKenna, R. Van Laer, A. H. Safavi-Naeini, Efficient bidirectional piezo-optomechanical transduction between microwave and optical frequency. *Nat.Commun.* **11**, 1166 (2020).
5. D. Li, Z. Bai, X. Zuo, Y. Wu, J. Sheng, H. Wu, Room temperature single-photon terahertz detection with thermal Rydberg atoms. *Appl. Phys. Rev.* **11**, 041420 (2024).
6. T. Xie, R. Fukumori, J. Li, A. Faraon, Scalable microwave-to-optical transducers at the single-photon level with spins. *Nat. Phys.* **21**, 931–937 (2025).
7. X. G. Zhang, Y. L. Sun, B. Zhu, H. W. Tian, B. Y. Wang, Z. Zhang, C.-W. Qiu, T. J. Cui, W. X. Jiang, Wireless microwave-to-optical conversion via programmable metasurface without DC supply. *Nat. Commun.* **16**, 528 (2025).
8. X. Liu, X.-M. Hu, T.-X. Zhu, C. Zhang, Y.-X. Xiao, J.-L. Miao, Z.-W. Ou, P.-Y. Li, B.-H. Liu, Z.-Q. Zhou, C.-F. Li, G.-C. Guo, Nonlocal photonic quantum gates over 7.0 km. *Nat. Commun.* **15**, 8529 (2024).
9. H. J. Kimble, The quantum internet. *Nature* **453**, 1023–1030 (2008).
10. J. Yang, M. Khanahmadi, I. Strandberg, A. Gaikwad, C. Castillo-Moreno, A. F. Kockum, M. A. Ullah, G. Johansson, A. M. Eriksson, S. Gasparinetti, Deterministic generation of frequency-bin-encoded microwave photons. *Phys. Rev. Lett.* **134**, 240803 (2025).
11. Y. Ma, Q. Zhang, H. Wang, 6G: Ubiquitously extending to the vast underwater world of the oceans comment. *Engineering* **8**, 12–17 (2022).
12. L. Li, X. Fan, G. Chen, Y. Liu, F. Zhang, Z. Chen, Z. Zhang, W. Xu, S. Zhang, Y. Liu, Z. Li, H. Gao, Z. Yan, W. Xiong, Q. Sun, From fish to fiber: 3D-nanoprinted optical neuromast for multi-integrated underwater detection. *Nat. Commun.* **16**, 7390 (2025).
13. H. Messer, A. Zinevich, P. Alpert, Environmental monitoring by wireless communication networks. *Science* **312**, 713 (2006).
14. C. Chen, X. Li, W. Li, M. Xue, Y. Shi, D. Dong, Y. Xu, Y. Liu, Y. Fu, Super-resolution acoustic displacement metrology through topological pairs in orbital meta-atoms. *Nat. Commun.* **15**, 8391 (2024).
15. H. Zang, Z. Xi, Z. Zhang, Y. Lu, P. Wang, Ultrasensitive and long-range transverse displacement metrology with polarization-encoded metasurface. *Sci. Adv.* **8**, eadd1973 (2022).

16. G. H. Yuan, N. I. Zheludev, Detecting nanometric displacements with optical ruler metrology. *Science* **364**, 771–775 (2019).
17. M. Sanz, U. L. Heras, J. J. García-Ripoll, E. Solano, R. Di Candia, Quantum estimation methods for quantum illumination. *Phys. Rev. Lett.* **118**, 070803 (2017).
18. D. G. England, B. Balaji, B. J. Sussman, Quantum-enhanced standoff detection using correlated photon pairs. *Phys. Rev. A* **99**, 023828 (2019).
19. H. Liu, D. Giovannini, H. He, D. England, B. J. Sussman, B. Balaji, A. S. Helmy, Enhancing LIDAR performance metrics using continuous-wave photon-pair sources. *Optica* **6**, 1349 (2019).
20. P. S. Blakey, H. Liu, G. Papangelakis, Y. Zhang, Z. M. Leger, M. L. Iu, A. S. Helmy, Quantum and non-local effects offer over 40 dB noise resilience advantage towards quantum lidar. *Nat. Commun.* **13**, 5633 (2022).
21. H. Liu, C. Qin, G. Papangelakis, M. L. Iu, A. S. Helmy, Compact all-fiber quantum-inspired LiDAR with over 100 dB noise rejection and single photon sensitivity. *Nat. Commun.* **14**, 5344 (2023).
22. Z. Wei, J. Jia, Y. Niu, L. Wang, H. Wu, H. Yang, Z. Feng, Integrated sensing and communication channel modeling: A survey. *Sci. China Inf. Sci.* **12**, 18850–18864 (2025).
23. X. Cao, H. Yang, Z.-L. Wu, B.-B. Li, Ultrasound sensing with optical microcavities. *Light Sci. Appl.* **13**, 159 (2024).
24. F. Xu, J. Shi, K. Gong, H. Li, R. Hui, B. Yu, Fiber-optic acoustic pressure sensor based on large-area nanolayer silver diaghragm. *Opt. Lett.* **39**, 2838 (2014).
25. H. Fan, L. Zhang, S. Gao, L. Chen, X. Bao, Ultrasound sensing based on an in-fiber dual-cavity Fabry-Perot interferometer. *Opt. Lett.* **44**, 3606 (2019).
26. L. Yang, C. Dai, A. Wang, G. Chen, D. Xu, Y. Li, Z. Yan, Q. Sun, Multi-channel parallel ultrasound detection based on a photothermal tunable fiber optic sensor array. *Opt. Lett.* **47**, 3700–3703 (2022).
27. H. Wei, Z. Wu, K. Sun, H. Zhang, C. Wang, K. Wang, T. Yang, F. Pang, X. Zhang, T. Wang, S. Krishnaswamy, Two-photon 3D printed spring-based Fabry-Pérot cavity resonator for acoustic wave detection and imaging. *Photonics Res.* **11**, 780–786 (2023).
28. P. Morris, A. Hurrell, A. Shaw, E. Zhang, P. Beard, A Fabry-Perot fiber-optic ultrasonic hydrophone for the simultaneous measurement of temperature and acoustic pressure. *J. Acoust. Soc. Am.* **125**, 3611–3622 (2009).
29. S. S. Kumar, C. A. Khansa, T. V. Praveen, C. V. Sreehari, T. Santhanakrishnan, R. Rajesh, Assessment of dynamic range in interferometric fiber optic hydrophones based on homodyne PGC interrogator. *IEEE Sensors J.* **20**, 13418–13425 (2020).
30. W. Xiong, Q. Shu, P. Lu, W. Zhang, Z. Qu, D. Liu, J. Zhang, Sensitivity enhanced fiber optic hydrophone based on an extrinsic Fabry-Perot interferometer for low-frequency underwater acoustic sensing. *Opt. Express* **30**, 9307–9320 (2022).
31. J. A. Guggenheim, J. Li, T. J. Allen, R. J. Colchester, S. Noimark, O. Ogunlade, I. P. Parkin, I. Papakonstantinou, A. E. Desjardins, E. Z. Zhang, P. C. Beard, Ultrasensitive plano-concave optical microresonators for ultrasound sensing. *Nat. Photonics* **11**, 714–719 (2017).
32. J. Ma, Y. He, X. Bai, L.-P. Sun, K. Chen, K. Oh, B.-O. Guan, Flexible microbubble-based Fabry–Pérot cavity for sensitive ultrasound detection and wide-view photoacoustic imaging. *Photonics Res.* **8**, 1558–1565 (2020).
33. L. Wang, Y. Zhao, B. Zheng, Y. Huo, Y. Fan, D. Ma, Y. Gu, P. Wang, Ultrawide-bandwidth high-resolution all-optical intravascular ultrasound using miniaturized photoacoustic transducer. *Sci. Adv.* **9**, eadg8600 (2023).
34. J. Ma, E. Fan, H. Liu, Y. Zhang, C. Mai, X. Li, W. Jin, B.-O. Guan, Microscale fiber photoacoustic spectroscopy for in situ and real-time trace gas sensing. *Adv. Photonics* **6**, 066008 (2024).
35. J. Guo, S. Xue, Q. Zhao, C. Yang, Ultrasonic imaging of seismic physical models using a phase-shifted fiber Bragg grating. *Opt. Express* **22**, 19573–19580 (2014).
36. W. Zhang, F. Chen, W. Ma, Q. Rong, X. Qiao, R. Wang, Ultrasonic imaging of seismic physical models using a fringe visibility enhanced fiber-optic Fabry-Perot interferometric sensor. *Opt. Express* **26**, 11025–11033 (2018).
37. G. Wu, L. Xiong, Z. Dong, X. Liu, C. Cai, Z.-m. Qi, Development of highly sensitive fiber-optic acoustic sensor and its preliminary application for sound source localization. *J. Appl. Phys.* **129**, 164504 (2021).
38. Z. H. Luo, B. Lu, J. L. Huang, C. Y. Ran, H. L. He, Sound source direction-of-arrival estimation method for microphone array based on ultra-weak fiber Bragg grating distributed acoustic sensor. *Opt. Express* **31**, 31342–31353 (2023).
39. T. Tan, X. Y. He, B. Chang, X. H. Guo, H. Zhou, Y. Geng, Y. Wu, Y. P. Liang, Z. P. Wang, Y. J. Huang, Y. Z. Yan, S. Q. Ge, Y. K. Su, C. W. Wong, B. C. Yao, Biomimetic acoustic perception via chip-scale dual-soliton microcombs. *eLight* **5**, 22 (2025).
40. S. Tian, P. Chen, M. Jiao, K. Mu, Y. Gao, Y. Qiao, L. Li, C. Shan, Geometry optimization of cantilever-based optical microphones. *Opt. Lett.* **49**, 2101–2104 (2024).
41. R. Ansari, E. Z. Zhang, A. E. Desjardins, P. C. Beard, All-optical forward-viewing photoacoustic probe for high-resolution 3D endoscopy. *Light Sci. Appl.* **7**, 75 (2018).
42. C. Zhang, T. Ling, S. L. Chen, L. J. Guo, Ultrabroad bandwidth and highly sensitive optical ultrasonic detector for photoacoustic imaging. *ACS Photonics* **1**, 1093–1098 (2014).
43. W. J. Westerveld, M. Mahmud-Ul-Hasan, R. Shnaiderman, V. Ntziachristos, X. Rottenberg, S. Severi, V. Rochus, Sensitive, small, broadband and scalable optomechanical ultrasound sensor in silicon photonics. *Nat. Photonics* **15**, 341–345 (2021).
44. J. Wang, P. H. Liang, J. Q. Song, P. Xu, Y. M. Hu, P. Zhang, K. Lou, R. Y. Ren, W. S. Tang, High-precision sub-wavelength motion compensation technique for 3D down-looking imaging sonar based on an acoustic calibration system. *Remote Sens.* **17**, 58 (2025).
45. Q. Zhang, Y. Wang, D. Li, J. Xie, K. Tao, P. Hu, J. Zhou, H. Chang, Y. Fu, Multifunctional and wearable patches based on flexible piezoelectric acoustics for integrated sensing, localization, and underwater communication. *Adv. Funct. Mater.* **33**, 202209667 (2023).
46. W. Zhang, R. Wang, Q. Rong, X. Qiao, T. Guo, Z. Shao, J. C. Li, W. Ma, An optical fiber Fabry-Perot interferometric sensor based on functionalized diaphragm for ultrasound detection and imaging. *IEEE Photonics J.* **9**, 7103208 (2017).

Acknowledgments: We thank X. Y. Zhou and F. Xu for helpful discussions. **Funding:** This work was financially supported by the National Key Research and Development Program of China (2023YFB2805700), the National Natural Science Foundation of China (grant nos. 62288101,12174187,92163216, 92150302, 92463308, and 12574356), the Natural Science Foundation of Jiangsu Province, China (grant nos. BK20240164 and BK20243009), and the Fundamental Research Fund for the Central Universities, China (grant no. 2024300329). **Author contributions:** C.S., H.L., and S.Z. conceived the project. X.Y. fabricated the samples. X.Y., Z.Z., and J.Z. conducted the experiments. X.Y., Z.Z., J.Z., C.S., L.L., X.L., H.L., and S.Z. analyzed the experimental and theoretical results. All authors contributed to discussions and writing of the paper. **Competing interests:** The authors declare that they have no competing interests. **Data, code, and materials availability:** All data and code needed to evaluate and reproduce the results in the paper are present in the paper and/or the Supplementary Materials. This study did not generate new materials.

Submitted 3 November 2025
Accepted 17 April 2026
Published 29 May 2026
10.1126/sciadv.adj6963

ScienceAdvances

Dual-function acoustic-to-optical transducers for underwater encrypted communication and subwavelength distance measurement

Xiao Yu, Jiaxuan Zhou, Zhiyao Zhang, Liangliang Lu, Xingsheng Luan, Chong Sheng, Shining Zhu, and Hui Liu

Sci. Adv. **12** (22), eadj6963. DOI: 10.1126/sciadv.adj6963